Catalysis Science & Technology

Accepted Manuscript

ROYAL SOCIETY OF CHEMISTRY

www.rsc.org/catalysis

Journal Name

ARTICLE

CeO_2 Nanodots Embedded in a Porous Silica Matrix as an Active yet Durable Catalyst for HCl Oxidation†

Received 00th January 20xx,
Accepted 00th January 20xx

DOI: 10.1039/x0xx00000x

www.rsc.org/

Xian Chen, [a, b] Xihua Xu, [a, b] Zhaoyang Fei, *[a] Xingxing Xie, [a] Jiawei Lou, [b] Jihai Tang, [b] Mifen Cui[b] and Xu Qiao * [b]

An unique architecture that the CeO_2 nanodots embedded in a porous SiO_2 matrix (CeO_2@SiO_2) was successfully fabricated by a spontaneous deposition strategy and evaluated in recycling Cl_2 from HCl oxidation. The nano-sized CeO_2 particles with a narrow size dstribution (2-4 nm) were uniformly dispersed in the amorphous SiO_2 matrix. Based on the characterizations of various techniques including XRD, SEM/(HR)TEM, H_2-TPR, Raman, XPS, it was revealed that the CeO_2 nanodots in the SiO_2 matrix exhibited significant "size effect", with the characteristics such as a considerably high concentration of Ce^{3+}, a high fraction of oxygen vancant sites, and a notably enhanced oxygen reducibility, which in turn affect on oxygen activation and surface Cl desorption. The current CeO_2@SiO_2 catalyst shows superior activity (1.60 $g_{Cl2}{\cdot}g_{cat}^{-1}{\cdot}h^{-1}$) and good durability (a time on stream of 100 h at 703 K). The isolation of fine CeO_2 nanodots by SiO_2 matrix is a key factor to inhibit the sintering of CeO_2 entities. Kinetic measurements indicate that catalytic activity is more dependent on the O_2 partial pressure than the HCl one, suggesting that enhancement in oxygen adsorption and surface Cl desorption is crucial for improving the cataltic activity.

Introduction

In view of the pressing concerns about environmental and energy issues, lots of researches are being directed to the heterogeneously catalyzed gas-phase oxidation of HCl, inevitably originating from the chlorine-related processes, for chlorine (Cl_2) recycle.[1] The introduction of the original $CuCl_2$/pumice catalyst by Deacon (Deacon process) in 1868 opened the course of Cl_2 production from HCl oxidation.[2] However, rapid catalyst deactivation due to the volatilisation of active phase is still insurmountable for copper-based catalytic materials, despite great efforts have been made on this catalytic system.[3-6] In the last decade, Sumitomo Chemicals has developed the efficient and stable RuO_2/TiO_2-rutile catalyst, which is considered as another milestone after Deacon process in the recovery of Cl_2 from HCl.[7-8] Although the RuO_2-based catalyst has sufficient performance as an industrial HCl oxidation catalyst, to attain a cheaper yet efficient catalyst is still highly desired because of the high and fluctuating price of the noble-metal ruthenium.[9, 10]

Ceria-based (CeO_2) materials have been claimed in patents as catalysts potentially suited for HCl oxidation.[11, 12] Recent studies have demonstrated that cost-effective CeO_2, which shows great resistance to bulk chlorination and a significant activity level, is an attractive alternative to RuO_2.[13] Intensive attentions have been triggered to the design of novel CeO_2 catalysts for oxidation of HCl.[14-16] The catalytic performance of CeO_2 depends strongly on its morphology, gain size, and existential state. It is well known that CeO_2 mixing with other metal oxides in the form of solid solutions can improve oxygen storage capacity compared to pure ceria and, thus, its performance.[17-22] The activity of $Ce_{0.5}Zr_{0.5}O_2$ obtained by a soft reactive grinding (SRG) method employed in our previous study is *ca*. 1.5 times higher than that of pure CeO_2.[14] On the other hand, the selection of a suitable support for the active phase can also tune its morphological and electronic properties and, in turn, catalytic performance. According to the early observations reported by Moser *et al.*, ceria can exhibit better performance in HCl oxidation when it was deposited in nano-sized form on specific ZrO_2 support. It was emphasized that the nanostructure of CeO_2 stabilized by ZrO_2 played a crucial role in improving the oxidation properties.[16]

In the current work, we present a novel method for the synthesis of CeO_2 nanodots with a uniform size embedded in porous silica matrix (CeO_2@SiO_2) under the synergistic interaction of the gelation of SiO_2 and *in situ* spontaneous deposition of CeO_2 induced by the hydrolysis of tetraethoxysilane (TEOS) and $Ce(NO_3)_3$, respectively. The process is facile and effective, and also easy for scale-up. Its physicochemical properties and catalytic performance in HCl oxidation were investigated and compared with pure CeO_2 and CeO_2/SiO_2 prepared by impregnation method. A kinetic study was systematically carried out to gain insights into the catalytic process. Moreover, this spontaneous deposition strategy is versatile for preparing other uniformly nano-sized inorganic materials.

Experimental section

Materials and Methods

[a] State Key Laboratory of Materials-Oriented Chemical Engineering, Nanjing Tech University, 5 Xinmofan Road, Nanjing 2100909, China.
E-mail: zhaoyangfei@njtech.edu.cn; Fax & Tel: +86 25 83587168;
[b] College of chemical Engineering, Nanjing Tech University, 5 Xinmofan Road, Nanjing 210009, China.
E-mail: qct@njtech.edu.cn; Fax & Tel: +86 25 83172298

† Electronic Supplementary Information (ESI) available: [additional supplementary figures]. See DOI: 10.1039/x0xx00000x

De-ionized water (18.0 MΩ) was used throughout experiments. Anhydrous ethanol (99.8 wt.%), TEOS (AR), $Ce(NO_3)_3·6H_2O$ (AR), acetic acid (AR), formamide (AR) and propylene oxide (C_3H_6O, AR) were supplied by Sinopharm Chemical Reagent Co., Ltd. High purity gases of N_2 (99.999%), Ar (99.999%), He (99.999%), and 10% H_2-Ar were supplied by Sanle Gas (Nanjing, China).

Catalyst preparation

The catalyst of CeO_2 nanodots embedded in a porous SiO_2 matrix (CeO_2@SiO_2) was prepared by a spontaneous deposition method. Typically, 60 mmol TEOS, 40 mmol $Ce(NO_3)_3·6H_2O$, and 125 ml ethanol were mixed and stirred at 298 K to yield a transparent solution (1). Then, a mixture of 82.5 ml de-ionized water and 125 ml ethanol was drop wise added into the transparent solution and the mixture was continuously stirred for 0.5 h. Subsequently, acetic acid (50 mmol) was dropped into the solution in 0.5 h. 100 ml C_3H_6O and 100 mmol formamide were also added with vigorous agitation, and the use of formamide is helpful to achieve uniform pore structure of architecture. The sample was sealed for about 0.5-1 h until gelation occurred. The gelation continued under the condition of reflux at ~348 K for 6 h. The obtained sample was aged in EtOH overnight at room temperature. The architecture of CeO_2@SiO_2 was obtained after drying at 333 K under vacuum for 48 h and calcination at 823 K in air for 4 h.

The catalyst of CeO_2 supported on porous SiO_2 (CeO_2/SiO_2) was prepared with an impregnation method involved two steps. The first step was the synthesis of carrier SiO_2, and the procedure was similar to that of the preparation of CeO_2@SiO_2, except without the addition of $Ce(NO_3)_3·6H_2O$ in the solution (1). The second step was the wet impregnation of porous SiO_2 substrate with an aqueous solution of $Ce(NO_3)_3·6H_2O$, followed by drying in an oven at 393 K for 24 h and calcination at 823 K in air for 4 h.

For comparison, pure CeO_2 was also prepared by thermal decomposition of $Ce(NO_3)_3·6H_2O$ at 823 K in air for 4 h.

Catalyst characterization

The amounts of Si and Ce in the solids were determined by inductively coupled plasma atomic emission spectroscopy (ICP-AES) using a Horiba Ultima 2 instrument equipped with photomultiplier tube detection. Powder X-ray diffraction (XRD) was used to characterize the phase structures of the samples. Measurements were performed on a SarmtLab X-ray Diffractometer (Rigaku Corporation, Japan), with Cu Kα radiation (λ=0.1541 nm) at 40 kV and 100 mA in a scanning range of 10-80° (2θ) with a step of 0.02°. N_2 isotherms were measured in a BEL sorp II apparatus at 77 K. The samples were evacuated at 573 K for 4 h prior to analysis. The specific surface area was calculated from the isotherms using the BET method. The average pore diameters and cumulative volume of pores were obtained by the BJH method from the desorption regimes of the isotherms.

SEM images were taken on a Hitachi S-3000N scanning electron microscope. Samples for SEM measurements were dispersed in ethanol by ultrosonication; drops of the suspension were applied onto substrates and dried in air. HRTEM images were taken using a JEOL JEM-2100 electron microscope operated at 200 kV. The laser Raman spectra were recorded at room temperature using a confocal microprobe JobinYvon Horiba LabRam HR800 Raman system with a spectral resolution of 2 cm^{-1} in a scanning range of 150-1000 cm^{-1}. The internal 514.5 nm line from He-Cd excitation was used as the source. The X-ray photoelectron spectroscopy (XPS) spectra were obtained at 298 K on a PHI 5000 Versa Probe high performance electron spectrometer with Al Kα (1486.6 eV) radiation as the excitation source at ultra-high vacuum (6.7×10^{-8} Pa). All binding energies (BE) were determined with respect to the C1s line (284.8 eV) originating from adventitious carbon. The powder samples were pressed into self-supporting disks loaded in the sub-chamber, and evacuated for 4 h. The deconvolution of XPS spectra was done by using Gaussian function.

H_2-TPR was performed in a fixed-bed quartz micro-reactor, using a mixture of 5 vol. % H_2/Ar as the reducing gas with a flow rate of 30 mL·min^{-1}. 50 mg catalyst was used in each measurement and pre-treated in Ar at 573 K for 1 h to remove the adsorbed species. After cooling down to room temperature, the reduction was performed from 323 to 823 K. The H_2 consumption during reduction was measured using a thermal conductivity detector (TCD). The TCD signal was calibrated by the quantitative reduction of Ag_2O to the metallic silver.

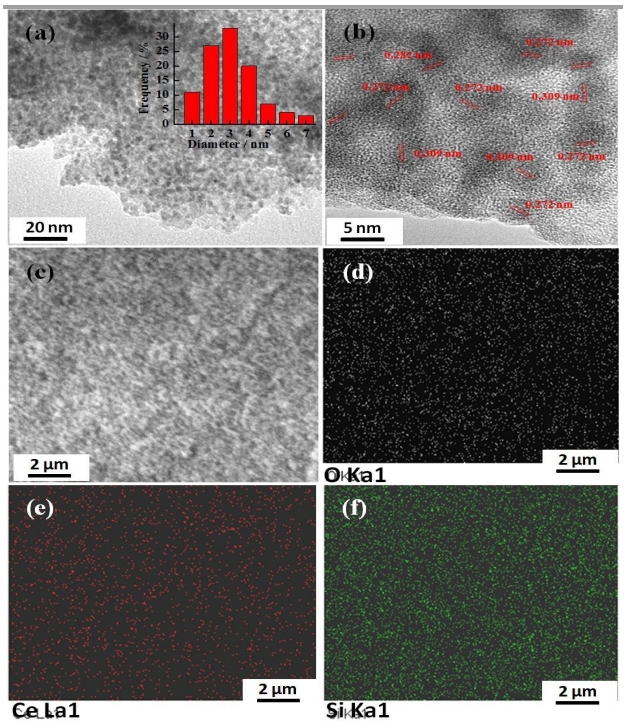

Figure. 1 (a, b) High-magnification TEM images of CeO_2@SiO_2, (c) Representative SEM image of CeO_2@SiO_2, and (d-f) elemental distribution of CeO_2@SiO_2 measured by mapping technique.

Catalyst evaluation and kinetic measurements

The catalytic activity test for HCl oxidation was carried out in a continuous flow fixed-bed quartz tube reactor (the equivalent diameter and length is 10 mm and 0.5 m, respectively) at atmospheric pressure. Catalyst (5 g) was loaded into reactor and then the reactor was first heated to 573 K under N_2 atmosphere to remove the adsorbed species on the catalysts. Then, the reaction feed (O_2/HCl = 2, v/v, and a flow rate = 240 ml·min^{-1}) was continuously introduced. The reaction temperature, measured by a thermocouple, was controlled in the range of 603 to 703 K at an interval of 20 K. The data obtained at each temperature was the average of three steady-state measurements. The chlorine balance was confirmed with an accuracy of ±3%. Blank experiments were conducted in an empty reactor which showed negligible activity in the adopted temperature range. The reaction mixture was absorbed by a potassium iodide solution in excess and analyzed by iodometry and acid-base titration to determine the amount of produced chlorine and unreacted HCl. The HCl conversion is calculated using the following equation (eq.1):

$$\text{HCl conversion } (\%) = \left\{1 - \frac{[\text{HCl}]_{out}}{[\text{HCl}]_{out} + 2[\text{Cl}_2]_{out}}\right\} \times 100 \qquad \text{eq. 1}$$

Where, HCl_{out} and Cl_{2out} are the moles of HCl and Cl_2 per minute in the effluent gas, respectively.

Kinetic measurements were performed under differential reaction conditions with typically 5 g catalyst. In order to limit the conversion to values between 5 and 20%, the catalyst samples were diluted with chemically inert SiO_2. Kinetic data were acquired after 60 min reaction time.

Results and discussion

Catalyst structure

Figure 1 a, b present representative TEM images of CeO_2@SiO_2 at high magnifications. One can see that CeO_2 nanodots are uniformly embedded in the silica matrix, and they are fairly monodispersed. Statistical analysis of the micrograph (Figure. 1 a) reveals that the size of CeO_2 nanodots ranges from 2 to 7 nm with an average diameter of ca. 3.0 nm. The high-magnification TEM image of CeO_2@SiO_2 clearly shows the crystalline nature of individual CeO_2 nanodots (Figure. 1 b). The interplanar distances with the *d*-spacings of 0.272 and 0.309 nm correspond to the (200) and (111) facets of cubic fluorite-type phase CeO_2, respectively. Meanwhile, amorphous SiO_2 around the CeO_2 nanodots could be observed. Figure 1 c presents the typical SEM image of CeO_2@SiO_2. The sample shows highly loose texture with uniform pore structures, which is further confirmed by the following N_2 sorption measurement. The elemental mapping results imply that all constituents are well distributed without zoning of CeO_2 (Figure 1 d-f). In view of micrographic observation of CeO_2@SiO_2, one may conclude that the architecture of CeO_2 nanodots embedded in the porous SiO_2 matrix was successfully developed by the spontaneous deposition strategy.

Table 1 BET surface areas, pore volumes, and pore diameters of the catalysts

Sample	BET surface area/$m^2 \cdot g^{-1}$	Pore volume /$cm^3 \cdot g^{-1}$	pore diameter /nm
CeO_2@SiO_2	474	0.50	4.3
CeO_2/SiO_2	227	0.24	3.8
CeO_2	48	0.06	5.0

Based on the N_2 sorption measurements of CeO_2@SiO_2 and CeO_2/SiO_2, the adsorption-desorption isotherms and the BET surface areas of the samples are presented in Figure 2 and Table 1, respectively. The isotherms of CeO_2@SiO_2 and CeO_2/SiO_2 are both type IV with H2-type hysteresis loops at a relatively low partial pressure region of P/P_0=0.4-0.8 (Figure 2), implying the existence of "ink-bottle" pore structure in both CeO_2@SiO_2 and CeO_2/SiO_2, formed by the agglomeration of the nanoparticle building blocks.[23, 24] The large pore volume of CeO_2@SiO_2 further demonstrates its highly loose texture, which was previously confirmed by the SEM observation. The BET surface area of CeO_2@SiO_2 is 474 $m^2 \cdot g^{-1}$, mainly originating from the porous SiO_2 matrix. This deduction can be further supported by a large surface area of a SiO_2 sample which

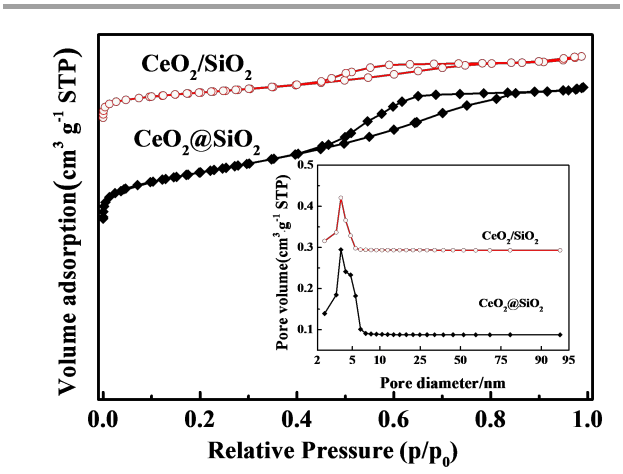

Figure. 2 N_2 sorption isotherms and pore size distribution curves (inset) of CeO_2/SiO_2 and CeO_2@SiO_2.

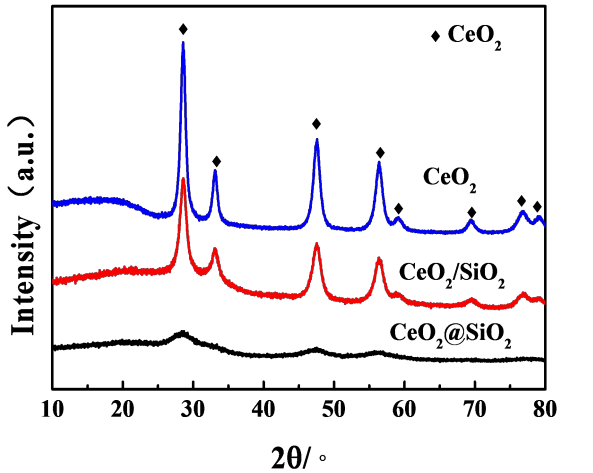

Figure. 3 XRD patterns of CeO_2@SiO_2, CeO_2/SiO_2, and CeO_2.

Table 2 Physico-chemical properties of the catalysts

Sample	*CeO_2 loading*[a] */wt.%*	*Grain size*[b] /nm	*Lattice parameter* /nm	FWHM /cm^{-1}	I_{600}/I_{460}	*H_2 Consumption*[c] /$cm^3 \cdot g_{cat}^{-1}$	*OSC* /$mg_{O2} \cdot g_{cat}^{-1}$
$CeO_2@SiO_2$	35	3.5	0.544	37.3	0.13	36.81	3.00
CeO_2/SiO_2	38	8.2	0.541	34.9	0.06	11.35	1.58
CeO_2	100	10.9	0.540	28.4	0.04	14.08	1.09

[a] Determined by ICP-AES analysis. [b] Particle size of CeO_2 based on XRD results. [c] H_2 consumption corresponding to the low-temperature reduction peaks (623-873 K).

was also prepared employing the same spontaneous deposition method (as high as 819 $m^2 \cdot g^{-1}$). Note that the surface area and the pore volume of CeO_2/SiO_2 is 227 $m^2 \cdot g^{-1}$ and 0.24 $cm^3 \cdot g^{-1}$, respectively. Compared to the SiO_2 support, the CeO_2/SiO_2 sample shows much smaller surface area and pore volume. This could be ascribed to the blocking of the pore structure of SiO_2 and/or creation of inaccessible internal hollows during the wet-impregnation procedure for preparing CeO_2/SiO_2. The pore size distribution curves (the inset of Figure 2) indicates that the average pore diameter of CeO_2/SiO_2 is ca. 3.8 nm, significantly smaller than that of SiO_2 (4.7 nm). $CeO_2@SiO_2$ exhibits a relatively narrow pore size distribution with an average pore diameter of ca. 4.3 nm.

According to the XRD patterns of the fresh $CeO_2@SiO_2$, CeO_2/SiO_2, and CeO_2 displayed in Figure 3, only the cubic fluorite-type phase CeO_2 can be identified (PDF-ICDD 34-0394). Obviously, the peaks of $CeO_2@SiO_2$ sample are relatively broad and weak. The size, distribution, crystallinity and quantity of CeO_2 could affect the XRD pattern of $CeO_2@SiO_2$ sample. Due to the calcination experience (823 K) and the high CeO_2 loading (35 wt%, confirmed by the following ICP-AES measurement) of $CeO_2@SiO_2$, the crystallinity or quantity of CeO_2 nanodots should not be an important issue. While according to the TEM/SEM results, the CeO_2 nanodots are 2~7 nm in size and well distributed on the SiO_2 substrates, which are the factors accounting for the relatively broad and weak CeO_2 peaks. (Figure. 1). CeO_2/SiO_2 and CeO_2 samples exhibite the sharp reflections, corresponding to the big CeO_2 grains (8.2, and 10.9 nm, respectively). The spontaneous deposition strategy is effective to achieve fine yet stable CeO_2 nanoparticles in the SiO_2 matrix. The calculated lattice parameter of ceria in $CeO_2@SiO_2$ is 0.543 nm, slightly larger than that of bulk CeO_2 (0.540 nm). The lattice expansion is likely resulting from a high fraction of the generated oxygen vacancies. [25, 26]

The XRD observations are well complemented by the Raman results. The Ceria materials generally exhibit the characteristic F_{2g} vibration band at 460 cm^{-1}.[27] Moreover, the FWHM of F_{2g} line was found to be related to the grain size of ceria: the bigger the value, the smaller the grain size.[28] Noticeably, the value of $CeO_2@SiO_2$ is indeed much bigger than those of CeO_2/SiO_2 and CeO_2, in consistent with the smaller size of $CeO_2@SiO_2$. The band at around 600 cm^{-1} is attributed to the oxygen vacant sites in the imperfect fluorite structure ceria.[29, 30] According to the I_{600}/I_{458} ratios (Table 2), it is clear that $CeO_2@SiO_2$ has the highest density of oxygen vacant sites among the three samples.

The reducibility of $CeO_2@SiO_2$, CeO_2/SiO_2, and CeO_2 was assessed by means of H_2-TPR. The H_2-TPR profiles are shown in Figure 5, and the quantitative H_2 consumptions corresponding to the reduction peaks in the 623 ~ 873 K range are summarized in Table 2. For pure CeO_2, peaks α_1, α_2 and β could be assigned to the reduction of surface oxygen species, subsurface layers of CeO_2, and bulk CeO_2, respectively.[31, 32] The reduction of CeO_2/SiO_2 is similar to that of pure CeO_2. The loading of CeO_2 onto SiO_2 via the impregnation approach shows a small impact on the reduction of different oxygen species. A weak Si-O-Ce interaction in CeO_2/SiO_2 may account for the observation. [33] In contrast, the reduction behaviour of $CeO_2@SiO_2$ is completely different. Only a broad peak (assigned to γ) centred at approximately 723 K can be observed over $CeO_2@SiO_2$,

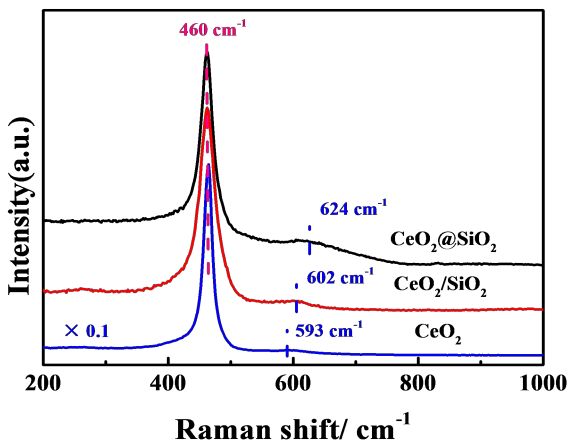

Figure 4 Raman spectra of $CeO_2@SiO_2$, CeO_2/SiO_2 and CeO_2.

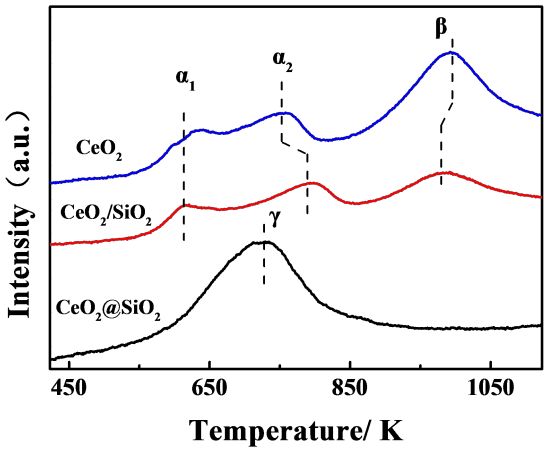

Figure 5 H_2-TPR profiles of $CeO_2@SiO_2$, CeO_2/SiO_2 and CeO_2.

Table 3 Surface atomic concentration of the catalysts

Sample	*Surface atomic concentration (%)*							
				Ce_T(%)		*O_T(%)*		
	O_T	*Ce_T*	*Si*	*Ce^{3+}/Ce_T*	*Ce^{4+}/Ce_T*	*O/O_T*	*O'/O_T*	*O''/O_T*
CeO_2@SiO_2	80.1	5.7	14.2	37.7	62.3	19.3	54.7	26.0
CeO_2/SiO_2	75.9	9.1	15.0	22.1	77.9	41.8	31.7	26.5
CeO_2	71.3	28.7	--	13.8	86.2	67.4	32.6	--

Ce_T total cerium; Ce^{3+}: trivalent cerium; Ce^{4+}: tetravalent cerium; O_T: total oxygen; O: lattice oxygen; O′: chemical adsorbed oxygen/weekly bonded oxygen; O″: oxygen in hydroxyl and surface adsorbed water.

implying the enhanced reducibility and mobility of oxygen in CeO_2@SiO_2. The low-temperature reducibility (623-873 K) of CeO_2 is associated with the formation of oxygen vacancies: the more susceptibly reducible a CeO_2 sample is, the easier it can generate oxygen vacancies. Therefore, it is clear that CeO_2@SiO_2 contains a high fraction of oxygen vacancies on the surface. The significantly enhanced reduction of CeO_2@SiO_2 could be associated with the small CeO_2 grain size. The surface atoms in the nanosized CeO_2 can be rather coordinatively unsaturated, leading to an enhancement in the reducibility of Ce^{4+}/Ce^{3+} couple associated with surface oxygen.[28] According to Table 2, CeO_2@SiO_2 has a deeper reduction as compared to CeO_2/SiO_2 and CeO_2. The determined values of the oxygen storage capacity (OSC) further support this conclusion. As a matter of fact, CeO_2@SiO_2 can store up to 3 times more oxygen than pure CeO_2 (Table 2), and it is worth pointing out that the total loading of CeO_2 in CeO_2@SiO_2 is only 35 wt.%.

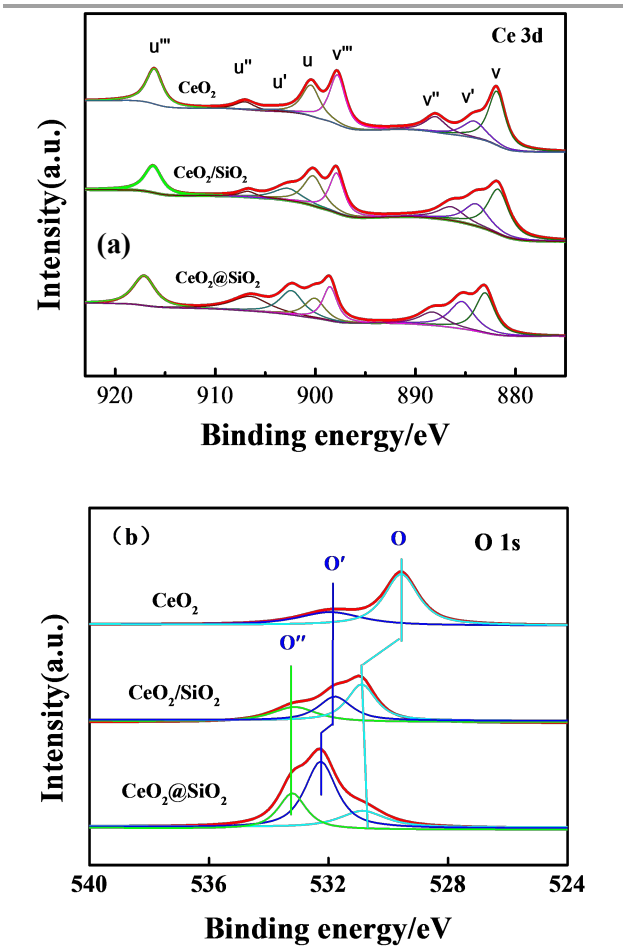

Figure 6 XPS spectra of CeO_2@SiO_2, CeO_2/SiO_2 CeO_2. (a) Ce 3d, (b) O1s.

The XPS characterization results are displayed in Figure 6. The whole spectra of Ce 3d was deconvoluted into eight components (Figure 6 a). The bands marked *u* are ascribed to the $3d_{3/2}$ spin-orbit states and those marked *v* are ascribed to the $3d_{5/2}$ states. The bands labelled *u′* and *v′* are ascribed to the primary photoemission of Ce^{3+} and the other six bands labelled *u‴* and *v‴*, *u″* and *v″*, and *u* and *v* are assigned to Ce^{4+}.[34, 35] The fitting results reveal that both Ce^{3+} and Ce^{4+} exist in the three samples, and the peaks attributed to Ce^{4+} are predominant. The presence of Ce^{3+} could create charge imbalance, resulting in the generation of oxygen vacancies, and unsaturated chemical bonds on the catalyst surface,[36] which further increases the amount of oxygen adspecies.[37] The surface element concentrations, the Ce^{3+}/Ce_T atomic ratios, and the surface fraction of different oxygen species are provided in Table 3. The Ce^{3+} content of CeO_2@SiO_2 (37.7%) is much higher than those of CeO_2/SiO_2 (22.1%) and CeO_2 (13.8%), and the sequence is consistent with that of OSC.

For the O1s spectra, the peaks in the 527.7-530.0 eV range could be attributed to lattice oxygen (O).[38-40] Two shoulders at the higher binding energy side can be ascribed to the chemisorbed oxygen and/or weakly bonded oxygen species (O′) as well as the oxygen in hydroxyl and/or surface adsorbed water (O″).[38, 40] As shown in Table 3, the total oxygen concentration and the fraction of O'/O_T on CeO_2@SiO_2 are also much greater than that of CeO_2/SiO_2 or CeO_2, which is thought to be associated with the higher surface concentration of Ce^{3+}, and responsible for the activity in oxidation reactions.[39]

Table 4 Reaction rates, activation energies (E_a) and reaction orders (HCl and O_2) of all catalysts.

Catalysts	*STY* [a]	r_A[b]	E_a	*Reaction Order*	
	$g_{Cl2}\cdot g_{cat}^{-1}\cdot h^{-1}$	$g_{Cl2}\cdot g_{CeO2}^{-1}\cdot h^{-1}$	$kJ\cdot mol^{-1}$	$\alpha(O_2)$	$\beta(HCl)$
$CeO_2@SiO_2$	1.60	4.58	58.8	0.48	0.48
CeO_2/SiO_2	1.18	3.11	62.1	0.36	0.48
CeO_2	1.01	1.01	69.6	0.31	0.49

[a] The space time yield defined as the gram of Cl_2 produced per gram of catalyst per hour. Conditions: T_{bed} = 703 K, O_2/HCl = 2:1 (v/v), W_{cat}/F_{HCl}= 0.03125 g·min·ml^{-1}. [b] Specific activities of HCl oxidation defined as the gram of Cl_2 produced per gram of ceria per hour. Conditions: T_{bed} = 703 K, O_2/HCl = 2, W_{cat}/F_{HCl}=0.03125 g·min·ml^{-1}.

The existing research examples suggested that the MVK mechanism can reasonably interpreter oxidation of HCl over the CeO_2-based catalysts. Previous studies on the CeO_2-based catalysts for HCl oxidation have also showed that features such as the concentration of oxygen vacant sites, the reducibility of CeO_2, and the textural structure have crucial impacts on HCl oxidation.[13, 14, 16, 41] More importantly, kinetic studies show that accelerating the replacement of surface Cl by O_2 is essential for improving the activity of CeO_2-based catalysts.[14] The HCl oxidation activity of the ceria catalysts fabricated in this work are evaluated and compared. As shown in Figure 7, the catalytic activities show the following order: $CeO_2@SiO_2 > CeO_2/SiO_2 > CeO_2$, which is in line with the Ce^{3+} concentration, the fraction of O′/O$_T$, and the reducibility of catalyst. Based on the STY of chlorine (per unit mass of catalyst) at 703 K, values of 1.60, 1.18, and 1.01 $g_{Cl2}\cdot g_{Cat}^{-1}\cdot h^{-1}$ are derived for $CeO_2@SiO_2$, CeO_2/SiO_2, and CeO_2, respectively. Further tests were conducted over $CeO_2@SiO_2$ at various conditions. Figure S1 shows that the highest STY of 2.10 $g_{Cl2}\cdot g_{cat}^{-1}\cdot h^{-1}$ can be achieved at the conditions of O_2/HCl = 1:1 (v/v) and W_{cat}/F_{HCl} =0.0156 g·min·ml^{-1}. The excellent performance of $CeO_2@SiO_2$ is also reflected in Table S1. The current $CeO_2@SiO_2$ certainly outperforms the other previously reported CeO_2-based catalysts under the similar reaction conditions. To assess the stability of $CeO_2@SiO_2$, a continuous reaction of 100 h was performed (Figure 8). Only approximately 5% loss of initial reactivity was observed over $CeO_2@SiO_2$ catalyst during the entire testing period, whereas nearly 50% loss of initial reactivity was found over CeO_2. TEM and XRD investigations on the used $CeO_2@SiO_2$ sample (Figures S2 and S3) revealed that the CeO_2 nanodots in $CeO_2@SiO_2$ are essentially maintained. The SiO_2 matrix may effectively isolate the fine CeO_2 entities which are thus prevent from sintering during the reaction.

Kinetic studies (the activity dependence on temperature, p_{O2} and p_{HCl}) were also conducted over $CeO_2@SiO_2$, CeO_2/SiO_2 and CeO_2. The HCl oxidation is a reversible reaction and can be strongly inhibited by products. To minimize the effect of reverse reaction, the conversion level is controlled between 5 and 20%. The apparent activation energies (*E*a) derived over $CeO_2@SiO_2$, CeO_2/SiO_2, and CeO_2 are found to be around 60 KJ·mol^{-1} (Figure. S4), indicating the same reaction mechanism of HCl oxidation over the three catalysts. Moreover, a relatively lower *E*a of $CeO_2@SiO_2$ (Table 4) may suggest an inherently high catalytic ability of this catalyst.

The reaction rate of HCl oxidation can be described as follows,

$$r_{HCl} = kP_{HCl}^{\alpha}P_{O_2}^{\beta} - k'P_{Cl_2}^{\gamma}P_{H_2O}^{\sigma}$$

Where, P_{HCl}, P_{O2}, P_{Cl2}, and P_{H2O} is the partial pressure of HCl, O_2, Cl_2, and H_2O, respectively. Here, the reverse reaction rate can be

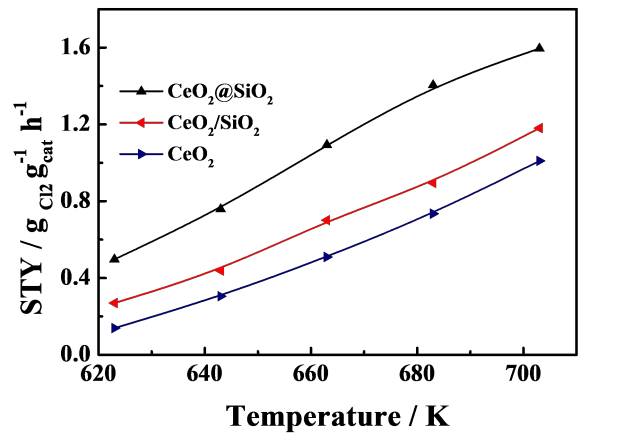

Figure 7 HCl oxidation over the three catalysts. Reaction conditions: O_2/HCl = 2:1 (v/v), W_{cat}/F_{HCl} = 0.0313 g·min·ml^{-1}.

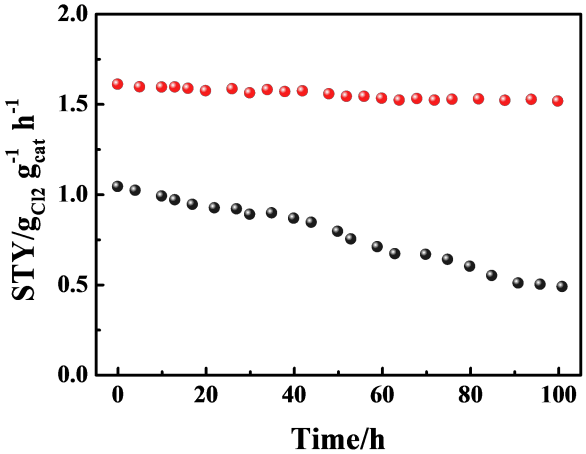

Figure 8 Catalyst durability tests on $CeO_2@SiO_2$ and CeO_2. Reaction conditions: T_{bed} = 703 K, O_2/HCl = 2:1 (v/v) and W_{cat}/F_{HCl} = 0.0313 g·min·ml^{-1}.

ignored. Then, a simplified and transformed equation was achieved:

$$\ln r_{HCl} = \ln k + \alpha \ln P_{HCl} + \beta \ln P_{O_2}$$

Special reaction rate were measured under different O_2 and HCl partial pressure. Then, the value of α and β can be derived from the slope of the fitted curve in Figure S5A and B, respectively. The reaction order with respect to O_2 and HCl was determined on CeO_2@SiO_2, CeO_2/SiO_2, and CeO_2, and the results are presented in Table 4. It was found that the activities of CeO_2@SiO_2, CeO_2/SiO_2, and CeO_2 will be enhanced by increasing the partial pressure of O_2 or HCl in the feed, which implies that both O_2 and HCl competed for the active sites rending desorption of surface Cl as the rate-determining step. [14] The reaction order with respect to HCl was found to be similar over the three catalysts, whereas a remarkable diversity in the reaction order with respect to O_2 was observed. The highest order of oxygen (0.48) over CeO_2@SiO_2 implies that an enhanced O_2 activation is benefit for the catalytic activity improvement.[42]

Conclusions

In summary, we reported for the first time in the current study the fabrication of uniform CeO_2 nanodots embedded in the SiO_2 matrix through a facile spontaneous deposition strategy. The CeO_2 nanodots in CeO_2@SiO_2 possessing a considerably high concentration of Ce^{3+}, a high fraction of O'/O_T, and a notably enhanced reducibility of catalyst. These features are closely associated with adsorption/activation of oxygen molecules, as well as desorption of surface Cl, and consequently impact on the catalytic activity of HCl oxidation. In comparison with the CeO_2-based catalysts reported in literature, the current CeO_2@SiO_2 catalyst shows superior activity (1.60 $g_{Cl2}\cdot g_{cat}^{-1}\cdot h^{-1}$) and good stability (a time on stream of 100 h at 703 K). The isolation of fine CeO_2 nanodots by SiO_2 matrix is effective to inhibit the sintering of CeO_2 entities.

Acknowledgements

Financial supports from the MSTC (Project No.2011BAE18B01), NSFC (Project No. 21306089) and HENSFJS (Project No. 13KJB530006) are greatly appreciated.

Notes and references

1 J. Pérez-Ramírez, C. Mondelli, T. Schmidt, O. F. K. Schlueter, A. Wolf, L. Mleczko, T. Dreier, *Energy Environ. Sci.* 2011，**4**，4786.
2 H. Deacon, US85370, 1868.
3 B. Neuman, *Angew. Chem.* 1915, **28**, 233.
4 F. Wattimena, W. M. H. Sachtler, *Stud. Surf. Sci. Catal.* 1981, **7**, 816.
5 C. Mondelli, A.P. Amrute, T.Schmidt, J. Pérez-Ramírez, *Chem.Commun.* 2011, **47**, 7173.
6 M. Hammes, H. Soerijanto, R. Schomäker, M. Valtchev, K Stöwe, W.F. Maier, *ChemCatChem* 2014, **6**, 245.
7 K. Iwanaga, K. Seki, T. Hibi, K. Issoh, T. Suzuta, M. Nakada, Y. Mori, T. Abe, *Sumitomo Kagaku* 2004-I, p. 1-11.
8 K. Seki, *Catal. Surv. Asia* 2010, **14**, 168.
9 A. P. Amrute, C. Mondelli, J. Pérez-Ramírez, *Catal. Sci. Technol.* 2012, **2**, 2057.
10 A. P. Amrute, F. Krumeich, C. Mondelli, J. Pérez-Ramírez, *Chem. Sci.* 2013, **4**, 2209.
11 X. Qiao, X. Chen, J. H. Tang, M. F. Cui, CN101357337A, 2009.
12 A. Wolf, L. Mleczko, O.F. Schlüter, S. Schubert, WO2010133313-A1, 2010.
13 A. P. Amrute, C. Mondelli, M. Moser, G. Novell-Leruth, N. Lopez, D. Rosenthal, R. Farra, M. E. Schuster, D. Teschner, T. Schmidt, J. Pérez-Ramírez, *J. Catal.* 2012, **286**, 287.
14 Z. Fei, X. Xie, Y. Dai, H. Liu, X. Chen, J. Tang, M. Cui, X. Qiao, *Ind. Eng. Chem. Res.* 2014, **53**, 19438.
15 M. Moller, H. Over, B. Smarsly, N. Tarabanko, S. Urban, *Catal. Today* 2015, **253**, 207.
16 M. Moser, C. Mondelli, T. Schmidt, F. Girgsdies, M. E. Schuster, R. Farra, L. Szentmiklósi, D. Teschner, J. Pérez-Ramírez, *Appl. Catal. B: Environ.* 2013, **132-133**, 123.
17 J. Li, X. F. Liu, W. C. Zhan, Y. Guo, Y. L. Guo, G. Z. Lu, *Catal. Sci. Technol.* DOI: 10.1039/C5CY01571E, 2015.
18 T. Yuzhakova, V. Rakić, C. Guimon, A. Auroux, *Chem. Mater.* 2007, **19**, 2970.
19 B. M. Reddy, P. Bharali, P. Saikia, S.E. Park, M.W.E. Van den Berg, M. Muhler, W. Grünert, *J. Phys. Chem. C* 2008, **112**, 11729.
20 B. Bonnetot, V. Rakić, C. Guimon, A. Auroux, *Chem. Mater.* 2008, **20**, 1585.
21 L. Liu, Z. Yao, B. Liu, L. Dong, *J. Catal.* 2010, **275**, 45.
22 H. Wang, X. Gong, Y. Guo, Y. Guo, G. Lu, P. Hu, *Angew. Chem. Int. Ed.* 2009, **48**, 8289.
23 K. S. W. Sing, D. H. Everett, R.A. Haul, L. Moscow, R.A. Pierotti, J. Rouquerol, T. Siemieniewska, *Pure Appl. Chem.* 1985, **57**, 603.
24 Z.Q. Zou, M. Meng, L.H. Guo, Y.Q. Zha, *J. Hazard. Mater.* 2009, **163**, 835.
25 J.F. Chen, J.J. Zhu, Y.Y. Zhan, X.Y. Lin, G.H. Cai, K.M. Wei, Q. Zheng, *Appl. Catal. A: Gen.* 2009, **363**, 208.
26 S. Sato, K. Koizumi, F. Nozaki, *J. Catal.* 1998, **178**, 264.
27 J. R. Mcbride, K. C. Hass, B. D. Piondexter, W. H. Weber, *J. Appl. Phys.* 1994, **76**, 2435.
28 L. J. Liu, Y. Cao, W. J. Sun, Z. J. Yao, B. Liu, F. Gao, L. Dong, *Catal. Today* 2011, **175**, 48.
29 Y. M. Choi, H. Abernathy, H. T. Chen, M. C. Lin, M. L. Liu, *ChemPhysChem* 2006, **7**, 1957.
30 N. Guillén-Hurtado, I. Atribak, A. Bueno-Lopez, A. García-García, *J. Mol. Catal. A: Chem.* 2010, **323**, 52.
31 M. J. Sun, G. J. Zou, S. Xu, X.L. Wang, *Mater. Chem. Phys.* 2012, **134**, 912.
32 W. Miśta, M.A. Malecka, L. Kępiński, *Appl. Catal. A: Gen.* 2009, **368**, 71.
33 W. R. Zhao, Y. Tang, Y. P. Wan, L. Li, S. Yao, X. W. Li, J. L. Gu, Y. S. Li, J. L. Shi, *J. Hazard. Mater.* 2014, **278**, 350.
34 S. Watanabe, X. L. Ma, C. S. Song, *J. Phys. Chem. C* 2009, **113**, 14249.

35 E. Bêche, P. Charvin, D. Perarnau, S. Abanades, G. Flamant, *Surf. Interface Anal.* 2008, **40**, 264.
36 Y. Zhang, A. H. Yuwono, J. Wang, J. Li, *J. Phys. Chem. C* 2009, **113**, 21406.
37 L. Chen, J. H. Li, M. F. Ge, *J. Phys. Chem. C* 2009, **113**, 21177.
38 X. Gao, Y. Jiang, Y. Zhong, Z. Luo, K. Cen, *J. Hazard. Mater.* 2010, **174**, 734.
39 S. Yang, W. Zhu, Z. Jiang, Z. Chen, J. Wang, *Appl. Surf. Sci.* 2006, 252, 8499.
40 Y. Eom, S. H. Jeon, T. A. Ngo, J. Kim, T. G. Lee, *Catal. Lett.* 2008, **121**, 219.
41 M. Moser, G. Vilé, S. Colussi, F. Krumeich, D. Teschner, L. Szentmiklósi, A. Trovarelli, J. Pérez-Ramírez, *J. Catal.* 2015, **331**, 128.
42 R. Farra, M. Eichelbaum, R. Schlögl, L. Szentmiklósi, T. Schmidt, A. P. Amrute, C. Mondelli, J. Pérez-Ramírez, D. Teschner, *J. Catal.* 2013, **297**, 119.

Table of Contents

CeO_2 Nanodots Embedded in a Porous Silica Matrix as an Active yet Durable Catalyst for HCl Oxidation

X. Chen, X. H. Xu, [a, b] Z. Y. Fei, X. X. Xie, J.W. Lou, J. H. Tang, M. F. Cui and X. Qiao**

The nano-sized CeO_2 particles (2-4 nm) with significantly rich surface defects and excellent redox ability uniformly embedded in the porous SiO_2 matrix exhibit superior and durable activity (1.60 $g_{Cl2} \cdot g_{cat}^{-1} \cdot h^{-1}$) with a time on stream of 100 h.